Ultramicroscopy 26 (1988) 361–376
North-Holland, Amsterdam

THE CONTRIBUTION OF INELASTICALLY SCATTERED ELECTRONS TO HIGH RESOLUTION IMAGES OF (Al, Ga)As/GaAs HETEROSTRUCTURES

C.B. BOOTHROYD and W.M. STOBBS

Department of Materials Science and Metallurgy, University of Cambridge, Pembroke Street, Cambridge CB2 3QZ, UK

Received 1 March 1988

In an analysis of the contributions which inelastically scattered electrons can make to the high resolution details of an electron microscope image, comparisons are made between experimental images with and without a centre-stop aperture and simulations which both neglect and include the expected inelastically scattered electrons. The simulations incorporating contributions from electrons which have undergone energy losses are, as described, only first-order approximations but of sufficient accuracy to demonstrate the importance of including such effects generally.

1. Introduction

The characteristics of an (Al, Ga)As/GaAs heterostructure which are needed for the improvement of such systems by device physicists and crystal growers are the Al content of the layers, their thickness, roughness and crystallographic misorientation. The most appropriate TEM techniques which can be used to obtain such data have been reviewed elsewhere [1,2]. For example, the Al content can be measured using 002 dark field images [3], but it now seems that to avoid systematic errors it is necessary to take account of differences in the inelastic scattering behaviour of the layers as function of their composition [4]. The layer thicknesses can also be determined to an accuracy dependent upon the objective aperture size used, provided the degree of crystallographic misorientation is known so that projection errors can be avoided [5]. The most difficult problem is the assessment of the form of any layer roughness, and this requires the measurement of individual interfacial step heights and spacings. This should be distinguished from the relatively easier evaluation of an inferred step density from the average layer misorientation determined using high resolution images. Equally, the projected diffuseness of an interface-whether caused by a gradation of the Al content, misorientation or inclined steps-can be measured to near atomic plane accuracy using Fresnel methods [6].

While AlAs and GaAs have very similar lattice parameters so that problems associated with foil-free surface relaxations for heterostructures of this system are unimportant [7], the main difficulty in using high resolution microscopy to determine the interface structure arises because changing the Al content causes only small changes in the scattering behaviour. This problem has been examined by a number of authors and is exacerbated by the fact that most heterostructures of device interest have an Al/As ratio of less than 0.3 [8]. It has been suggested that there are advantages in examining the interface at the cube normal [9,10], but if the resolution is improved, as is necessary, by allowing 022 * as well as 200 reflections to contribute to the image, the contrast between the layers tends to decrease [11,12]. Images showing fairly large differences in visibility of the layers have been obtained by several authors at both (110) and (100) normals for pure AlAs/GaAs heterostructures and certain specific thickness ranges (e.g., refs. [13,14]). However, a feature of the compari-

* In this paper we take the layer normal to be (001) and an "edge-on" specimen used to examine the layering to have a surface normal of (100).

0304-3991/88/$03.50

sons of computed and experimental images is that the latter tend to exhibit lower layer visibilities than expected [14] even though the effects of absorption are now frequently included in the computations (e.g., refs. [14–16]). In an attempt to improve layer visibility while retaining high resolution we have suggested that it should be advantageous to exclude the 000 beam using a centre-stop aperture in the diffraction plane so as to form an axial high resolution "dark field" image [17]. The technique has now been used with some degree of success [18], but the image character exhibited is not generally as expected. As we will demonstrate here, the reasons for this have their origin in the atomic level detail which can be contributed to an image by multiple inelastic/elastic scattering, and that this is so indicates (as discussed in section 3) that the quantitative analysis of high resolution images will have to be treated with considerably more caution than has hitherto been considered necessary.

2. Computational methods

Multislice calculations were performed on a 6×1 periodically continued supercell of three $Al_{0.3}Ga_{0.7}As$ and three GaAs unit cells, neglecting upper Laue zone contributions and sampling the scattered amplitude in a 256 by 32 point array. For this sampling the supercell used proved to be close to the maximum possible size for the avoidance of "wrap-around" effects during the fast Fourier transforms. The form of the calculations was that developed from the more basic multislice calculations of Maclagan et al. [19]. Microscope parameters appropriate for the Cambridge high resolution electron microscope operated at an accelerating voltage of 500 kV were used; under these conditions Scherzer defocus is at $\Delta f = -62$ nm.

Inelastically scattered electrons were included using a program written in Semper [20]. Electrons that have lost energy will be focussed more strongly by the objective lens than purely elastically scattered electrons and will form a more-overfocus image. Thus inelastically scattered electrons were included by the addition of image intensity at different defoci weighted according to the form of a calculated energy loss profile. This full profile was obtained by convoluting an energy spread function (of Gaussian form with a full width at half maximum of ~ 6 eV) with a delta function at zero loss together with a plasmon peak at ~ 16 eV energy loss (equivalent to $\Delta f \simeq +100$ nm) of Lorentzian form with a full width at half maximum of 3 eV ($\equiv \Delta f \simeq 18$ nm). This form for the energy loss profile is sufficiently similar to that observed experimentally to allow realistic inferences on those characteristics of an image which might be associated with the effects of such losses, as is the requirement here, but experimental forms would be used for full fitting procedures if these were required. It should be noted that in the image simulations reported here the inelastic contribution is taken to arise from electrons which are inelastically scattered and then elastically scattered over the *full* specimen thickness. This is only a first-order approximation for the real way in which multiple scattering occurs throughout the specimen thickness. If a fully quantitative comparison with experimental data were required, the type of calculation described could be treated as a "module" for a more accurate simulation with electrons progressively being fed from the elastic to the "inelastic/elastic" calculation as a function of specimen thickness. Given that, as we will see, we were more concerned with fitting features of experimental images which were not predicted *at all* by elastic calculations; the first-order calculation used was considered to be sufficiently accurate for the purposes of this paper, and requires much less computer time than a fully quantitative approach.

The effects of the typical angular distribution of inelastically scattered electrons at the energy losses considered and at an accelerating voltage of 500 kV are much less than would be expected at lower accelerating voltages, as has been analysed elsewhere [21] and simulations including the angular distribution expected (from, e.g., ref. [22]) for the losses used also showed that it could be neglected in our first-order calculations. Furthermore, since the calculations described here were designed to demonstrate the effects of the *addition* of inelastic contrast, the effects of absorption were neglected, but could obviously also be included (in

modified form) for fully accurate quantitative comparisons. It is interesting that the neglect of phonon scattering effects is not in any way limiting, since in this case the angular distribution is sufficiently broad to prevent such loss-electrons from contributing significant atomic resolution detail [21].

3. Simulation description

As will be seen, we were interested primarily in the interpretation required for "centre-stop" images but we will first assess the effects on the bright field 100 cube normal interface image of changes in specimen thickness and resolution, assuming that the contrast arises from only elastically scattered electrons.

Simulated images of an $Al_{0.3}Ga_{0.7}As/GaAs$ interface as a function of thickness and defocus for an objective aperture with an Airy function resolution limit of 0.21 nm (022 beams excluded) are shown in fig. 1a, and similar simulations for a 0.18 nm resolution cut-off (022 beams included) are shown in fig. 1b. The changes in layer contrast can be understood by referring to the amplitudes and phases of the beams as a function of specimen thickness as plotted in fig. 2. Thus, when the 022 beams are excluded (fig. 1a) the layer visibility is generally higher for most specimen thicknesses than when these beams are included. At this point it is worth distinguishing between the effects on the layer visibility of changes in the image contrast and in the mean image intensity. The mean *intensity* for a given area of image takes the local variations in intensity to be smeared out to a uniform grey. The mean is thus proportional to the sum of the *intensity* of the beams contributing to that image area, and for a simulation of a uniform crystal with no beams excluded by an objective aperture it is always equal to the incident intensity, provided absorption is ignored. Also, far from an interface, where the interface Fresnel effects do not affect the image, the mean intensity is independent of defocus. The image *contrast* represents the magnitude of the atomic scale variations in intensity and is proportional to the difference in intensity between the adjacent black and white blobs. Image contrast is produced by the interference of two or more beams and so depends on their amplitudes as well as on how their relative phases are changed by the objective lens transfer function. The overall layer visibility in a multilayer is governed by a combination of the changes across the interface in the mean image intensity and contrast as well as, in some cases, the *form* of the interference pattern. In order to perform valid comparisons of intensity and contrast between images at different thicknesses and defoci all the simulations within each figure have been printed on the same intensity scale. We now see that in fig. 1a for thicknesses up to about 23 nm the mean image intensity is roughly the same for GaAs and (Al, Ga)As because, although the 002 beams are more intense for (Al, Ga)As, the 000 beam is correspondingly less intense. However, the (Al, Ga)As and GaAs layers can still be distinguished because of the much greater image contrast of (Al, Ga)As which results from the greater amplitude of the (Al, Ga)As 002 beams interfering with the 000 beam. At a thickness of 41 nm the intensities of both the 000 and 002 beams for (Al, Ga)As are greater than those for GaAs, so that the layer visibility is now enhanced by the greater mean intensity of the (Al, Ga)As layer (given that, for these simulations, the 022 beams are excluded). When the 022 beams are included, as for fig. 1b, there is no enhancement of the visibility of the higher thickness from *intensity* differences.

Examining in more detail the differences in appearance of the (Al, Ga)As and GaAs with a resolution cut-off at 0.18 nm we see from the simulations (fig. 1b) that although the 022 beams differ in amplitude for (Al, Ga)As and GaAs for thicknesses above about 23 nm, this does not improve the layer visibility when these beams are allowed to contribute to the image using a 0.18 nm aperture (as in fig. 1b) because of the related reductions in intensity of the 000 beam so that the mean image *intensity* for the two layers is relatively unchanged. At the lowest specimen thicknesses ($\leqslant 14$ nm) the layer visibility is negligible, by comparison with the situation when only 002 beams contribute, because the 022 amplitudes then dominating the image are comparable for

(Al, Ga)As and GaAs and the 002 amplitudes are small. It is only once the strongly composition-dependent 002 beam amplitudes become significant that the *pattern* differences between the materials allow their recognition. Indeed for the higher resolution, and increasingly for greater thicknesses, the main way in which the different layers can be recognised is through such differences in the pat-

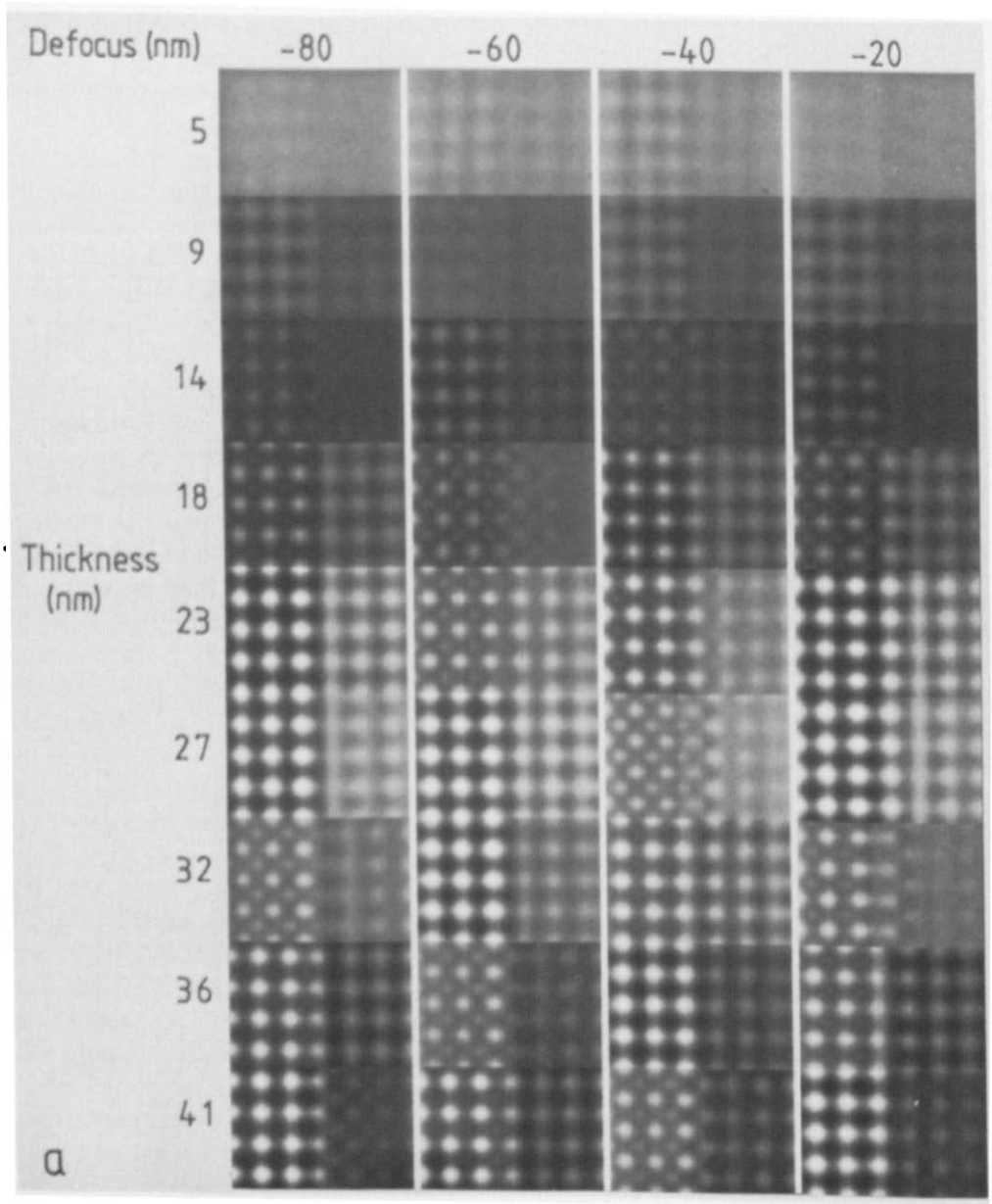

Fig. 1. Simulated images of a $Al_{0.3}Ga_{0.7}As/GaAs$ interface (GaAs on the right) imaged with the beam parallel to [100] and assuming that only elastically scattered electrons contribute. In these and all following image simulations each image is calculated with the same intensity scale relative to the incident electron beam intensity (= 1) and is printed with zero electron intensity as black. The electron intensity corresponding to white is given for each figure. The resolution cut-off for (a) is 0.21 nm (022 beams excluded) and white = 2, so that intensities from 2 up to the maximum of 2.9 appear as white. For (b) the resolution cut-off is at 0.18 nm (022 beams included), white = 3 and intensities from 3 to 5.4 are now white. For (c) the cut-off is again at 0.18 nm but now the 000 beam is excluded and white = 2, so that intensities from 2 to 3.8 are white.

tern of interference contrast which is itself increasingly complicated by non-linear contributions.

If it is sought to improve the layer visibility by excluding the 220 beams and so increasing the intensity difference, then unfortunately the resolution is limited (linearly) to 0.21 nm. This is insufficient to determine the structure around a step in an (Al, Ga)As/GaAs interface, and the original motivation for the work described here was to determine conditions under which this could be done. In order to determine a step structure, information from the 022 and preferably the 004 beams is needed while at the same time sufficient layer visibility (whatever its origin) is retained to distinguish the atomic columns on either side of the boundary. Incidentally, it should be noted that approaches which rely on Fourier filtering (e.g., ref. [15]), while allowing easier *recognition* of a

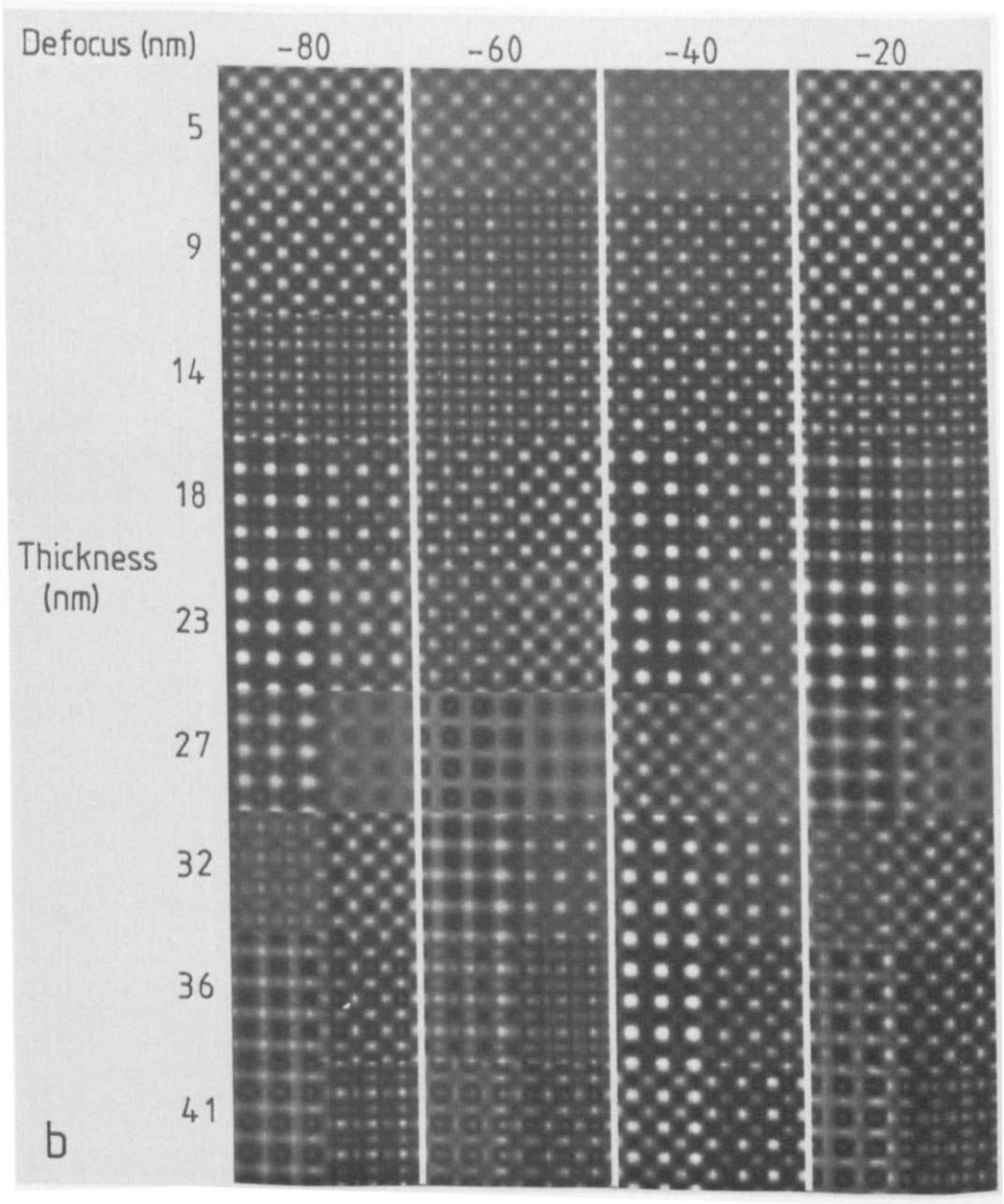

Fig. 1 (continued).

step, will preclude its accurate structural analysis. Excluding the 000 beam but allowing all other beams to contribute to the image should improve the layer visibility and still retain the resolution. Accordingly, simulations are presented in fig. 1c for an $Al_{0.3}Ga_{0.7}As/GaAs$ interface imaged under conditions similar to fig. 1b, but with the 000 beam excluded by a centre-stop aperture of radius 0.6 nm. It can be seen that the layer visibility predicted is much greater than for fig. 1b, particularly for specimen thicknesses around 27 nm. This is because, at this thickness, the 022 beam is at a minimum intensity, so that the mean image intensity is determined mainly by the 002 beam intensity. For higher thicknesses, the 022 beam intensity for GaAs is greater than that for (Al, Ga)As,

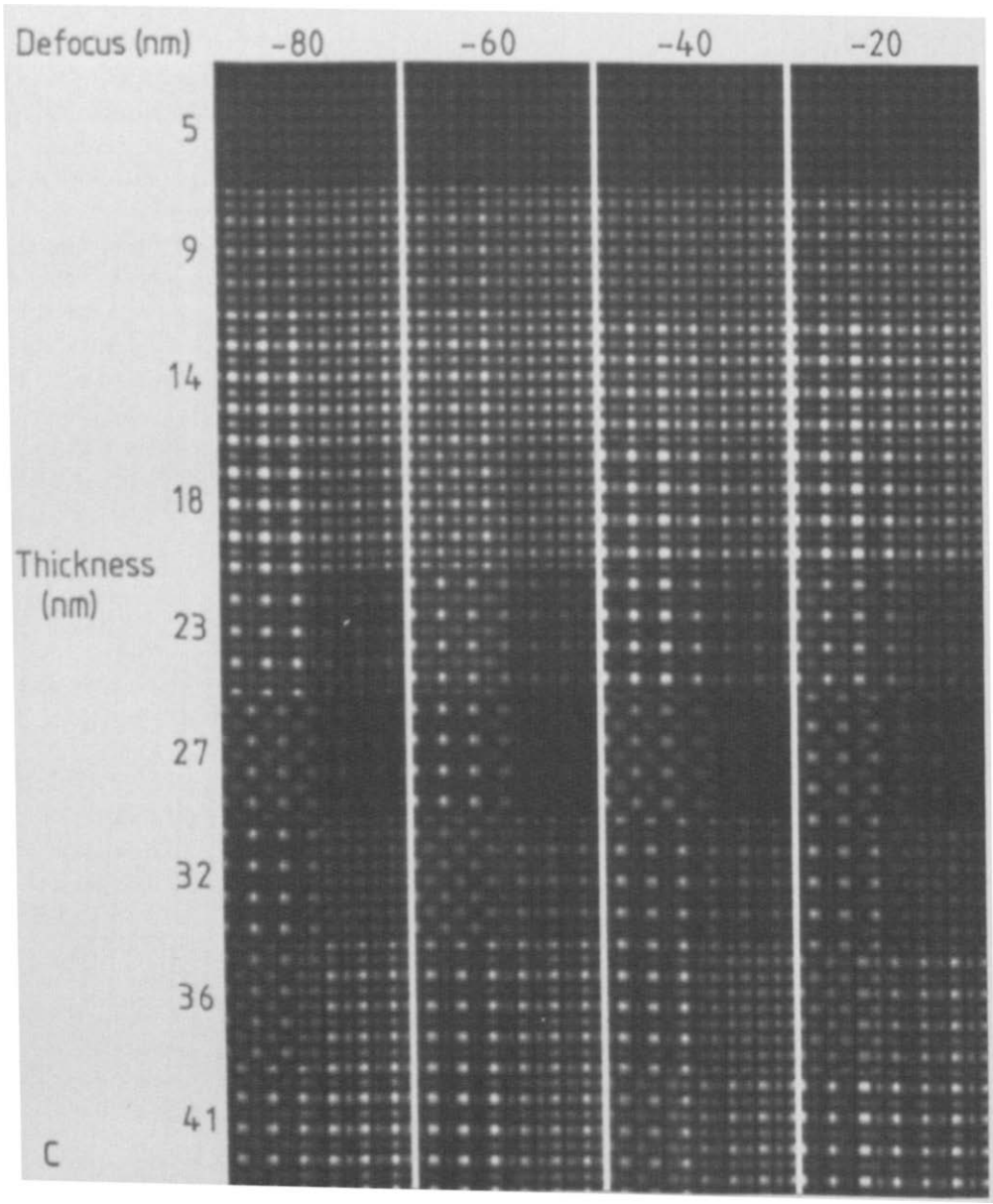

Fig. 1 (continued).

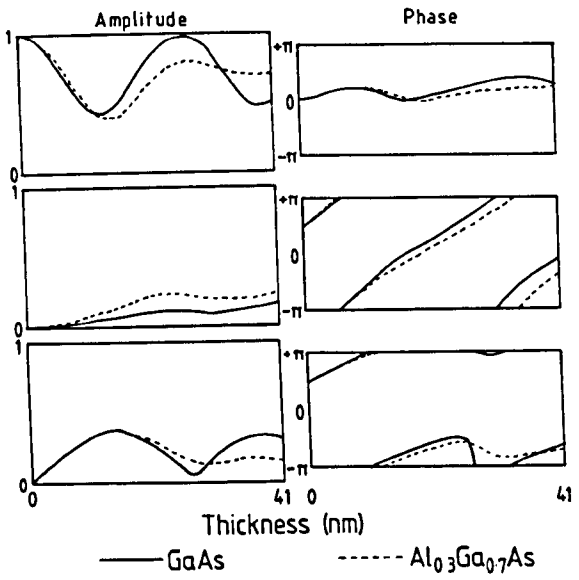

Fig. 2. Amplitudes and phases of the 000, 002 and 022 beams at [100] for $Al_{0.3}Ga_{0.7}As$ and GaAs as a function of thickness.

compensating for the 002 beam intensity differences, so that again layer visibility is now retained only through pattern differences.

It is possible to increase the layer visibility, at least in centre-stop dark field images, by tilting a few degrees away from the exact [100] beam direction about the layer normal (001) so that the interface normal remains perpendicular to the beam. The layer visibility is increased by tilting because the four 022 beams and the 020 and $0\bar{2}0$ beam intensities are decreased: the image is then dominated by the 002 and $00\bar{2}$ beams. Simulations for an $Al_{0.3}Ga_{0.7}As$/GaAs interface tilted by 4.3° about [001] are shown in fig. 3 both without (a) and with (b) a centre-stop aperture. The centre-stop image simulations (fig. 3b) now show the 0.14 nm fringes parallel to the interface which arise from the interference of the 002 and $00\bar{2}$ beams, and images of this type can be obtained experimentally, though with considerable difficulty [18].

The simulations of figs. 1 and 3 suggest that the layer visibility of (Al, Ga)As/GaAs multilayers should be greatly increased when the 000 beam is excluded by a centre-stop aperture, both when the beam is parallel to [100] and when tilted a few degrees away from [100]. It is therefore rather disconcerting to find that the layers in experimental centre-stop dark field images are usually indistinguishable, the images showing a remarkable and general lack of similarity to the simulations! Experimental bright field and centre-stop dark field images of an (Al, Ga)As/GaAs multilayer taken with the beam tilted slightly away from [100] are shown in fig. 4. The layers are totally invisible in fig. 4a (right) (which was taken at approximately Scherzer defocus) and only became visible (fig. 4a (left)) for an *overfocus* of about 180 nm relative to fig. 4b. The centre-stop dark field images (fig. 4b) show no layer contrast at all and are dominated by 0.28 nm fringes, even at the thinnest part of the specimen. The main features of the experimental centre-stop images are that they exhibit no contrast reversals (black dots changing to white) as a function of specimen thickness and that the mean intensity increases monotonically with thickness. The simulations at [100] show a contrast reversal and a minimum in the mean intensity at about 27 nm thickness which is lost on tilting (fig. 3b), and this at least is consistent with the image appearance. However, the experimental images are remarkably similar over a wide range of defocus with 0.28 rather than 0.14 nm fringes, and the middle of the optimum defocus range is considerably underfocus relative to the Scherzer defocus value.

In seeking a possible explanation for why the centre-stop dark field images (fig. 4b) are so different from the simulations with (fig. 3b) or without (fig. 1c) a small specimen tilt we must now consider the possible effects which could derive from inelastic scattering contributions. It is clear that whilst the incoherent inelastic scattering of electrons and their subsequent addition to the image as a constant background could explain some of the reduction in layer visibility [15], high resolution detail must be contributed by inelastic scattering if the persistence of the 0.28 nm fringes is to be explained in the centre-stop images. This can arise as a result of the subsequent elastic diffraction of initially inelastically scattered electrons *, and the loss electrons most likely to form

* A temporal sequence should not be taken literally and is used in our description of the processes for convenience.

a reasonably strong lattice image are those that have undergone plasmon or lower single electron excitation losses since such electrons have a small angular distribution [22]. Image simulations similar to fig. 1c (assuming zero angular spread) with a centre-stop aperture but including the effects of inelastic scattering are shown in fig. 5.

The proportion of electrons that are taken to be inelastically scattered was determined for each thickness using an inelastic cross-section of 1.633

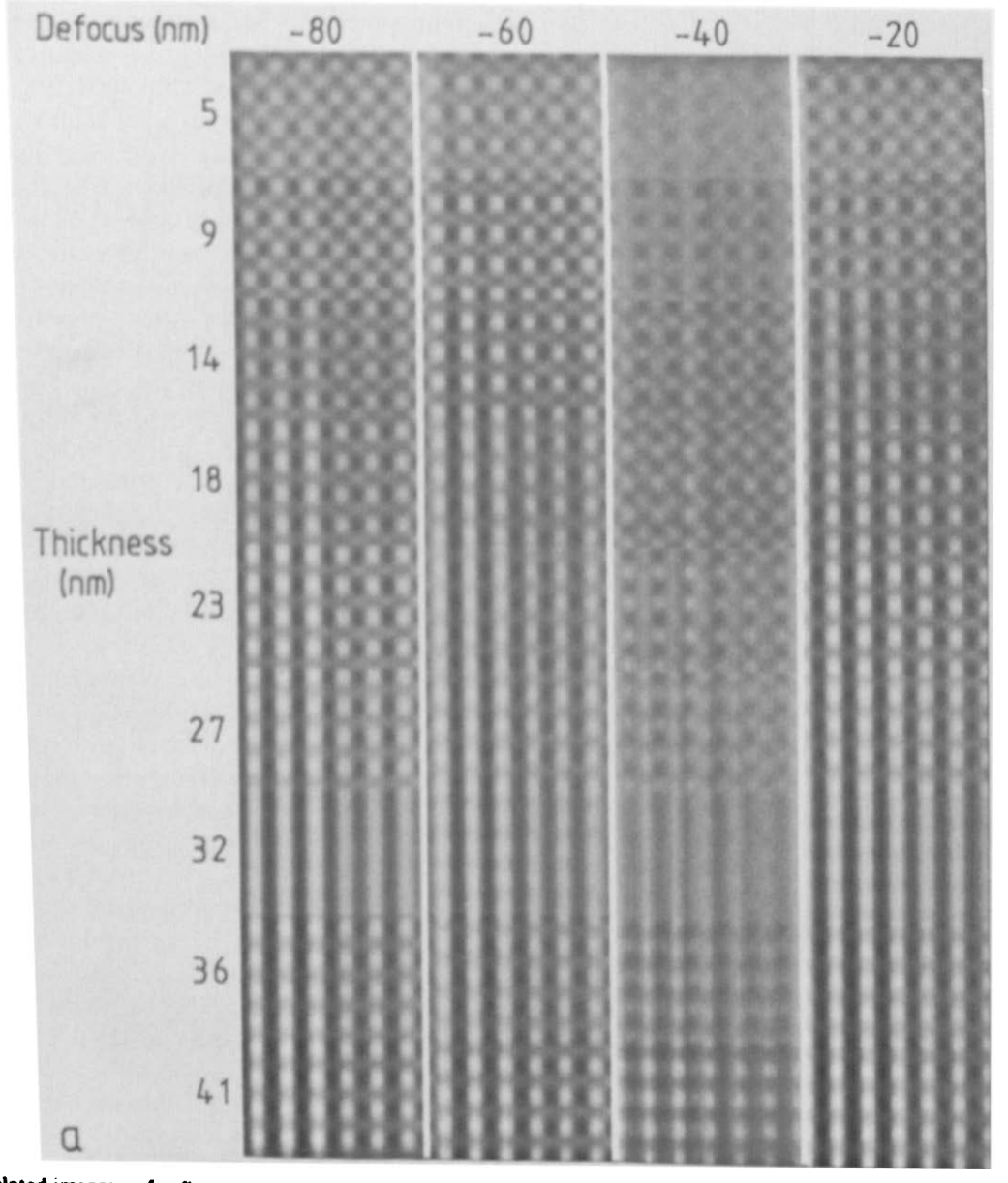

Fig. 3. Simulated images as for fig. 1b with a 0.18 nm resolution cut-off but with the specimen tilted by 4.3° about [001]. For (b) the 000 beam is excluded with an *inner* cut-off at 0.6 nm. For (a) white = 2 and intensities from 2 to 2.2 appear as white. For (b) white = 0.3 and intensities from 0.3 to 0.36 appear as white. Note that (a) is dominated by 0.28 nm fringes parallel to the interface whereas in (b) the fringes are predominantly of 0.14 nm spacing. The layer visibility with the centre stop (b) is high for all thicknesses.

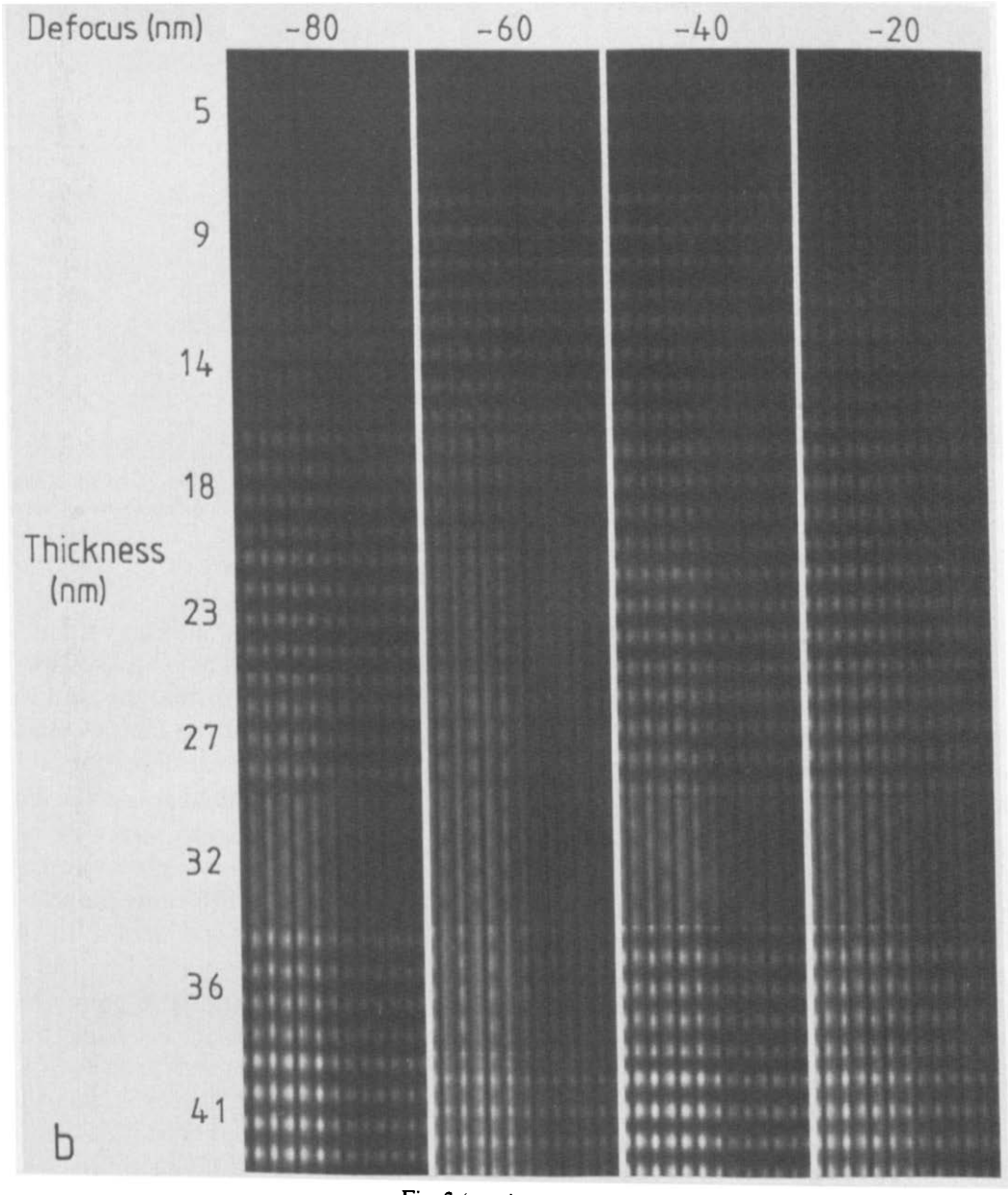

Fig. 3 (continued).

$\times 10^{-4}$ nm^2. Thus, for example, at a thickness of 32 nm the simulations in fig. 5 were obtained by the incoherent addition of a simulation assuming solely elastic scattering for 79% of the electrons and assuming an inelastic loss distribution as described in section 2 for 21% of the electrons. This approach was taken for all the conditions where the effects of inelastic scattering were included, and no account was taken of "primary" inelastic sources in the Bragg scattered beams.

It can be seen that the inclusion of inelastic scattering produces only a small reduction in the difference of the mean intensities across the interface at the (100) normal, but the details of the image are changed more significantly, with an increase in emphasis on the non-linear contribu-

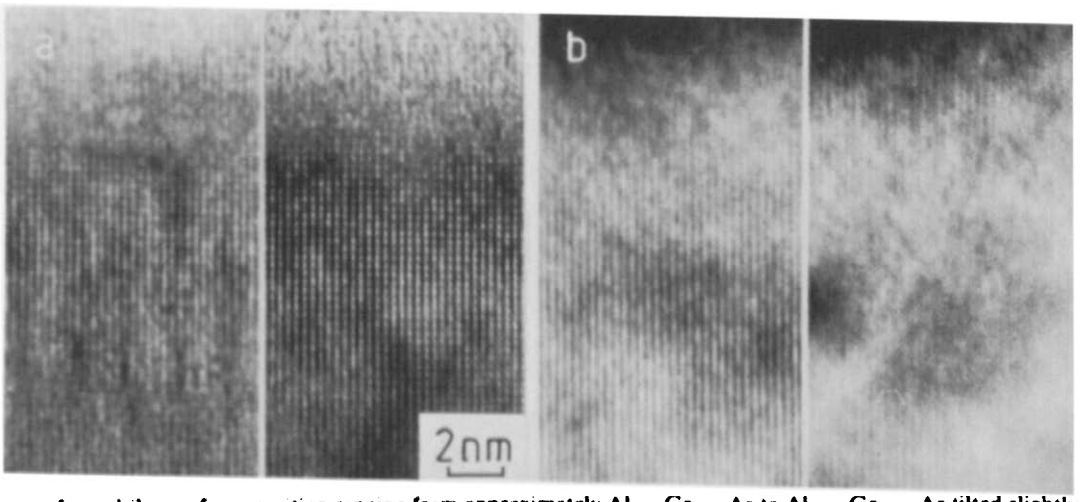

Fig. 4. Images of a multilayer of composition ranging from approximately $Al_{0.15}Ga_{0.85}As$ to $Al_{0.35}Ga_{0.65}As$ tilted slightly about the layer normal [001] using (a) no aperture and (b) a centre-stop aperture. The change in defocus between the two images is about 180 nm for both (a) and (b).

tions due to 002/020 interferences. This is evident as a brightening of the fainter white spots (cf. fig. 1c) and is particularly visible for a thickness of 27 nm at −20 nm and −60 nm defocus and for 41 nm thickness at higher defoci. The reasons for the relative enhancement of the non-linear terms when inelastically scattered electrons are included are discussed in more detail elsewhere [21] but are the same as those which lead to a similar effect if the *incident* electrons exhibit an increased energy spread. It is effects of this type due to inelastic scattering which render invalid the early ideas on the use of centre-stop images [23,24] to distinguish linear and non-linear contributions [21]. As a result of these changes in the contributions to the image the exact defoci at which high resolution contrast reversals take place are slightly altered and become less visible. It should be noted that this would make the use of such thickness matches for a wedge of known angle, so as to provide a measure of the Al content, highly inaccurate. The low resolution intensity changes across an interface in a cleaved wedge as viewed at the cube normal have been used to provide an apparently sensitive measure of Al content [25,26]. In an otherwise elegant analysis, the effects of absorption on the thickness fringes were not included, and while this is obviously necessary, the analysis here suggests that the effects of *contributions* from inelastically scattered electrons should also be incorporated for accurate analysis work.

Since it is now clear that the addition of contributions to the centre-stop image simulations deriving from inelastic scattering for a (100) beam direction (fig. 5) do not explain the appearance of the experimental images, we must now examine the possibility that an explanation for the image appearance (with 0.28 nm fringes) requires a specimen tilt (which *is* evident in fig. 4) as well as these inelastic contributions. The centre-stop simulations shown in fig. 6 were thus obtained again including inelastic scattering, but now for a 4.3° specimen tilt as was used for fig. 3b. Comparing fig. 6 with fig. 3b, the effect of the inelastic scattering with a tilted crystal is mainly to reduce the mean intensity difference between the layers, and this is consistent with the relatively low layer visibility seen experimentally when 0.14 nm lattice fringes are observed [18]. However, the effects of inelastic scattering as predicted above are generally to *enhance* the smaller fringe spacings, and this is obviously completely contrary to the observed dominance of the larger 0.28 nm fringe spacings found in the experimental images reported here (fig. 4b).

Experimentally the only remaining possible difference in the conditions used for those centre-stop dark field images which show 0.14 nm lattice

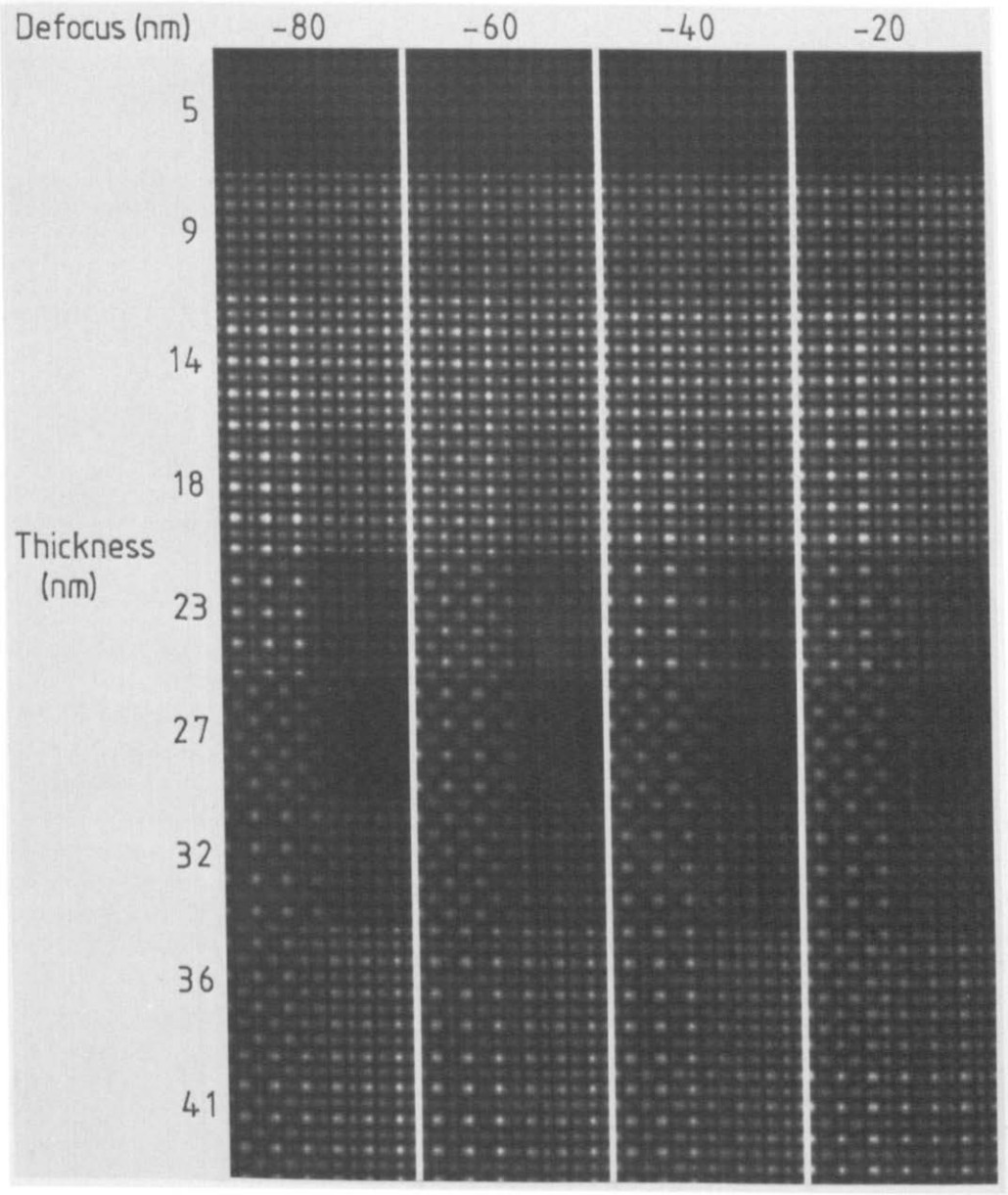

Fig. 5. Simulations as for figure 1c with a centre-stop aperture but including inelastically scattered electrons. Their effect is to enhance the 0.14 nm spacing over the 0.28 nm spacing (thus reducing the visibility of pattern contrast reversals) and is particularly noticeable at the higher thicknesses (white = 2 and intensitities from 2 to 2.9 are white).

fringes reported elsewhere [18] and those in fig. 4b with 0.28 nm fringes lies in the beam convergence which was used in each case. For example, the convergence used for the images in fig. 4b was set by increasing the convergence until it was evident that electrons were just passing the edge of the centre stop in the absence of specimen scattering. The convergence was then decreased a little to about 2 mrad. While a convergence of this magnitude has been demonstrated to be unimportant in its effect on the resolution at 500 kV, we can see that it is possible for a proportion of the electrons which are inelastically scattered by a relatively much smaller angle to pass by the edge of the centre stop. These would then form a hollow-cone "bright field" image by multiple inelastic/elastic

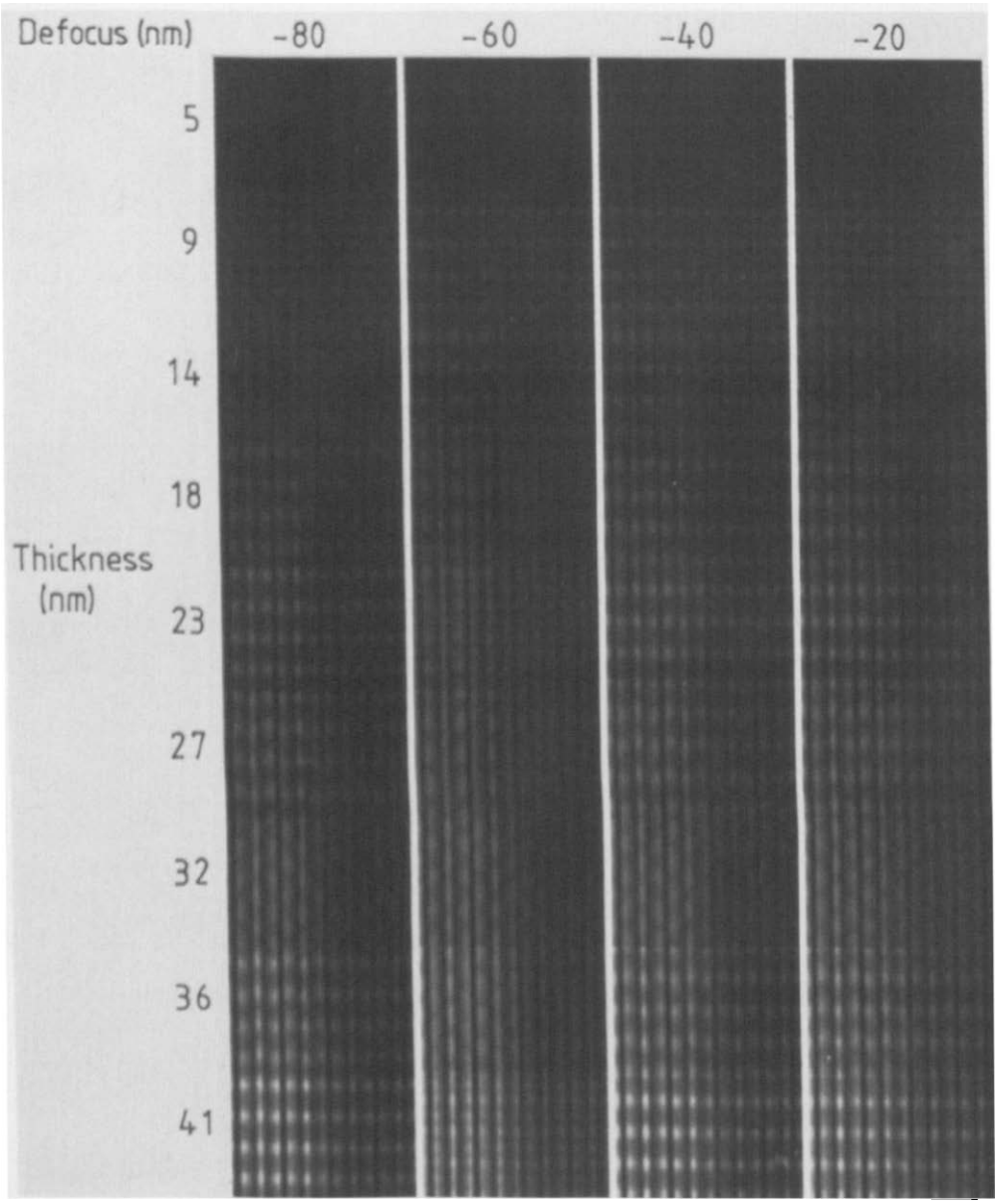

Fig. 6. Simulations as for figure 3b with a centre-stop aperture and a tilted beam but including inelastically scattered electrons in correctly increasing proportion as a function of thickness. Their effect is to decrease the layer visibility, but the 0.14 nm fringes remain (white = 0.3).

scattering despite the presence of the centre stop. Such an image *would* contain 0.28 nm fringes similar to those seen in fig. 3a due to the interference of the 000 and 002 beams. Furthermore, the effects of the hollow-cone nature of the transfer would qualitatively be expected to reduce the dependence on defocus (e.g., ref. [27]) as is experimentally observed. A precise simulation of an image including the angular distribution of both elastically and inelastically scattered electrons would require the addition of many images calculated with the beam direction both inside and outside the centre-stop aperture and is thus precluded. However, a first-order approximation to how the images are built up under these circumstances is shown in fig. 7 for a $Al_{0.3}Ga_{0.7}As/$

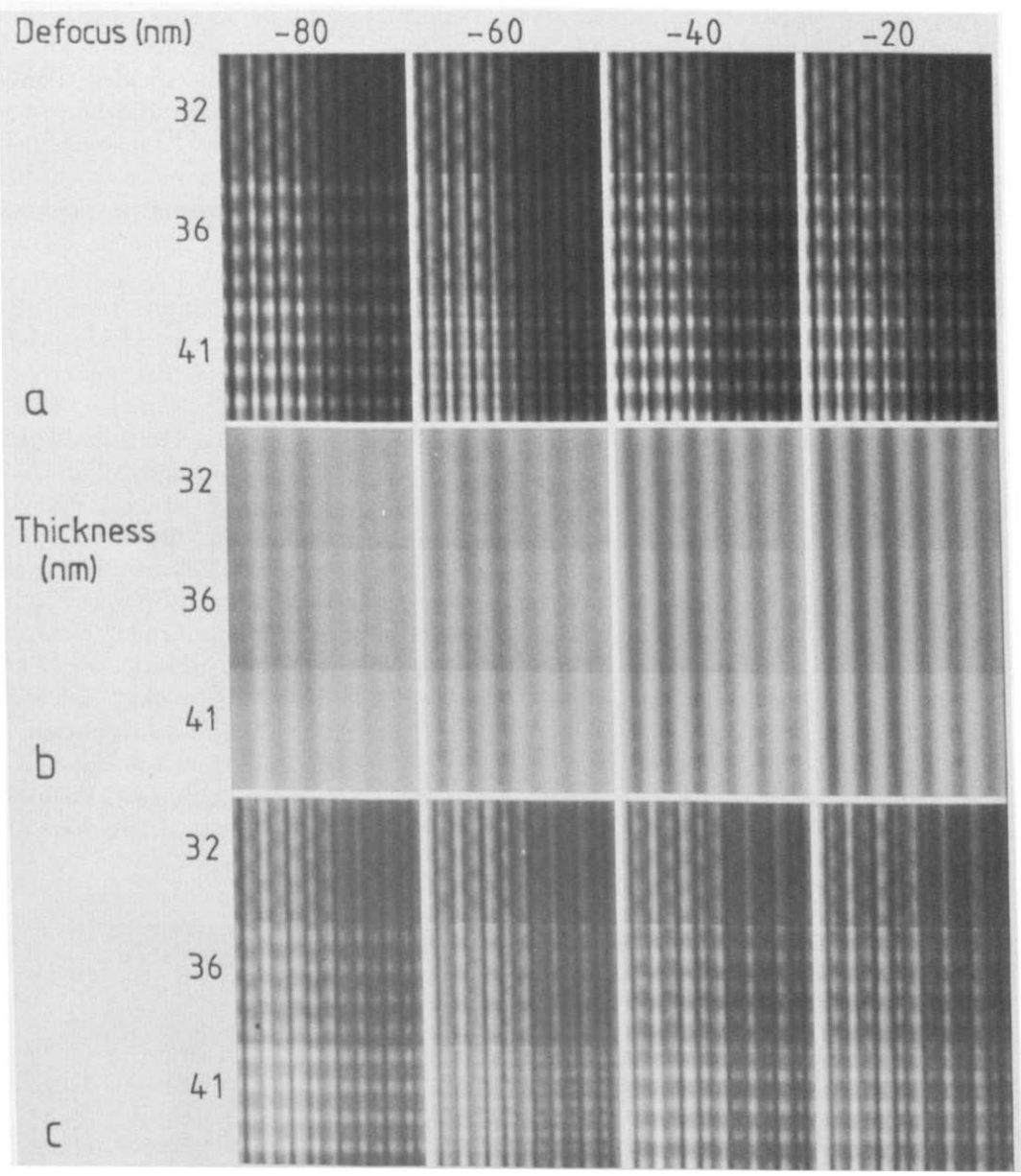

Fig. 7. Simulated images for the centre-stop configuration with a specimen tilt of 4.3° as for fig. 6. Here in (a) we add only half the inelastically scattered electrons as a contribution to a dark field image. (b) shows the contribution made by the remainder as a hollow-cone bright field image, and (c) is the sum of both inelastic contributions (in a comunally increasing proportion as the thickness is increased) to the normal elastic centre-stop image. For (a) and (b) white = 0.2 and intensities from 0.2 to 0.24 appear white while for (c) white = 0.35, intensities from 0.35 to 0.39 appearing white.

GaAs interface tilted 4.3° from [100]. We make the approximation that half of the inelastically scattered electrons evade the centre-stop aperture to form a hollow cone *bright* field image since the convergence used was about 0.3 mrad less than the aperture centre-stop semi-angle: for a Lorentzian distribution of the scattering with a cut-off of about 2.7 mrad [22] this fraction provides a reasonable estimate. The remaining inelastically scatter electrons will form a *dark* field centre-stop image of the same type that we have already described. These inelastic hollow-cone

bright field images were simulated by adding six images calculated with a beam tilt of 2.4 mrad (so that the 000 beam passed the centre-stop aperture of radius 2.3 mrad) distributed at 60° intervals around the centre stop. Fig. 7a shows the image formed from *just* the decreasing proportion with thickness of solely elastically scattered electrons together with the increasing proportion of the inelastic electrons scattered *within* the centre-stop aperture and thus also forming a *dark* field image. These images are similar to fig. 6 except that they contain contributions from only half the inelastically scattered electrons. The effect of the other half of the inelastically scattered electrons distributed around the centre stop is shown in fig. 7b and is the sum of the six tilted *bright* field images. It can be seen that the inelastic contribution in fig. 7b is now dominated by 0.28 nm fringes and the (Al, Ga)As and GaAs layers are now indistinguishable, whereas the mainly elastic contribution (fig. 7a) is dominated by 0.14 nm fringes. Fig. 7c is the sum of figs. 7a and 7b and it can be seen that the inelastic scattering around the centre-stop aperture both greatly reduces the layer visibility and enhances the 0.28 nm fringe spacing. Whilst it must be remembered that fig. 7c can only be considered to be a first approximation to the effects of inelastic scattering around the centre stop, since neither the incident convergence nor the angular inelastic spread is known accurately, it is encouraging that fig. 7c matches the experimental observations much more closly than does fig. 3b. That the experimental images in fig. 4b are indeed dominated by inelastic scattering, as the above qualitative match suggests, is further reinforced by the fact that the range of defoci over which lattice fringes are visible in the centre-stop images is generally further underfocus than for conventional bright field images. This is as would be expected given that electrons with less energy are focussed more strongly than zero-loss electrons at a given lens excitation, though the effects of beam-stop charging cannot be precluded.

The importance of electrons scattered inelastically around the centre stop in contributing to fig. 4b can be further confirmed experimentally by reducing the incident-beam convergence and thus the relative magnitude of the "hollow-cone bright field inelastic/elastic" contribution. An image taken in this way is shown in fig. 8. Now the 0.14 nm $00\bar{2}$ $\bar{0}02$ fringes are clearly visible, in qualitative agreement with the simulations of fig. 5 (for

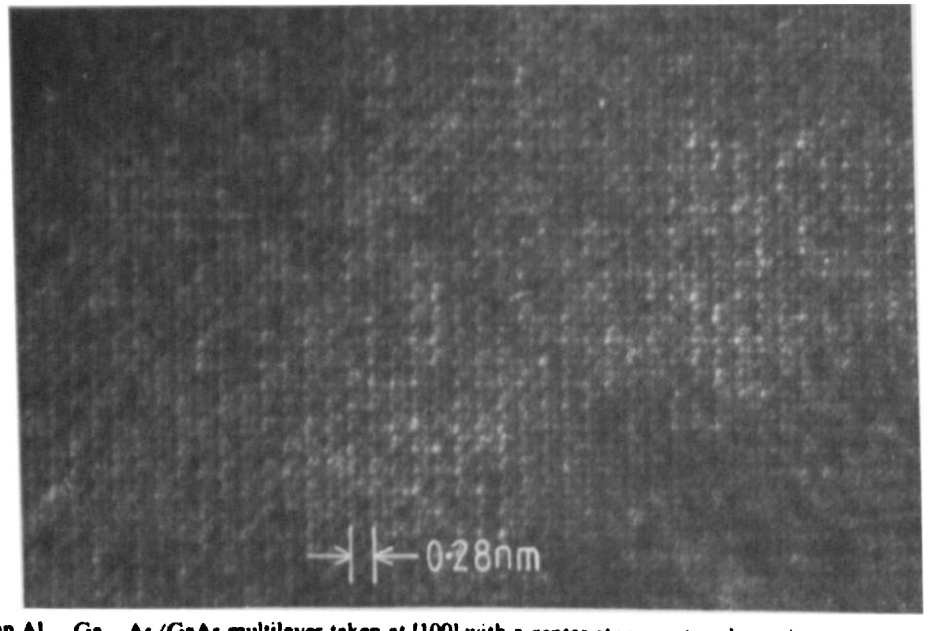

Fig. 8. Image of an $Al_{0.3}Ga_{0.7}As/GaAs$ multilayer taken at [100] with a centre-stop aperture but using a much lower incident beam convergence than used for fig. 4b.

which the incident convergence was zero) for a thickness of about 18 nm. Furthermore, the way the 0.28 nm fringes remain, with at least as high a contrast as the 0.14 nm fringes, suggests that comparison with simulations such as those for fig. 7 would allow the determination of the relative magnitudes of the different contributions if this were desired.

4. Conclusion

Given that the contrast in centre-stop dark field images can be derived, as we have demonstrated, only when the contribution due to inelastically scattered electrons is included, it is clear that inelastic scattering *must* make a major contribution to *conventional* bright field high resolution images as well as to centre-stop dark field images. Typical exposure times for the dark field centre-stop images are only about a factor of two or so higher than for bright field images, and typical cross-sections for low-angle inelastic scattering are, of course, comparable to elastic cross-sections for low atomic number ($Z \sim 10$) elements. Whilst the relatively different absorption of electrons for the different materials (in this case (Al, Ga)As and GaAs) undoubtedly contributes to changes in the difference between the mean intensities of the layers in a multilayer, it is clear that the subsequent elastic scattering of inelastic electrons can contribute to the detail of a high resolution image. Furthermore, if contributions from inelastically scattered electrons are included in an image simulation, the effects of phenomenological absorption would have to be treated in a modified way. Determining the structure and composition at steps in (Al, Ga)As/GaAs interfaces requires the quantitative matching of high resolution images with simulations, and this will require more accurate simulation of the inelastic contributions to the image than we have attempted here, as well as careful analysis either experimentally or theoretically of the angular distribution of the electrons undergoing the relevant range of energy losses. For centre-stop dark field images it is possible, as has been demonstrated, to reduce the inelastic contributions to the image by reducing the incident beam convergence (but at the expense of longer exposure times), but it would be better to increase the diameter of the centre-stop aperture to prevent electrons from being scattered around it. However, such methods do not, of course, prevent inelastic scattering from occurring and will thus allow only a qualitative interpretation of the images produced without considerable improvements in the simulation procedure again to include the multiple inelastic/elastic contributions which will necessarily remain. It would appear that the accurate quantitative analysis of interfacial step structure will have to wait until an energy-filtering high resolution electron microscope becomes available. This conclusion is further strengthened for interfacial structure analysis more generally when it is remembered that the inelastic cross-section would be expected to be locally dependent upon the interfacial defect structure.

In summary, the principal result reported here is the experimental demonstration of the significant atomic-level detail contributed to a high resolution image by inelastic loss electrons, as predicted in previous analyses [21].

Acknowledgements

We are grateful to the SERC and to Philips Research Laboratories (Redhill) for financial support and to Dr. J. Gowers for discussion and for provision of the specimens examined.

References

[1] E.G. Britton, K.B. Alexander, W.M. Stobbs, M.J. Kelly and T.M. Kerr, GEC J. Res. 5 (1987) 31.
[2] W.M. Stobbs, in: Proc. 3rd Intern. Conf. on Modulated Semiconductor Structures (MSS-III), Montpellier, 1987 (J. Physique 48 (1987) C5-33).
[3] P.M. Petroff, J. Vacuum Sci. Technol. 17 (1980) 1128.
[4] E.G. Britton, PhD Thesis, University of Cambridge (1987).
[5] C.B. Boothroyd, E.G. Britton, F.M. Ross, C.S. Baxter, K.B. Alexander and W.M. Stobbs, in: Microscopy of Semiconducting materials, 1987, Inst. Phys. Conf. Ser. 87, Ed. A.G. Cullis (Hilger, Bristol, 1987) p. 15.
[6] F.M. Ross, E.G. Britton and W.M. Stobbs, in: EMAG '87, Ed. G.W. Lorimer (Institute of Metals, London, 1988) p. 205.

[7] M.M.J. Treacy, J.M. Gibson and A. Howie, Phil. Mag. A51 (1985) 389.
[8] M.J. Kelly, in: The Physics and Fabrication of Microstructures and Microdevices, Springer Proceedings in Physics, Vol. 13, Eds. M.J. Kelly and C. Weisbuch (Springer, Berlin, 1986) p. 174.
[9] Y. Suzuki and H. Okamoto, J. Appl. Phys. 58 (1985) 3456.
[10] C.J.D. Hetherington, J.C. Barry, J.M. Bi, C.J. Humphreys, J. Grange and C. Wood, in: Layered Structures, Epitaxy and Interfaces, 1984, Mater. Res. Soc. Symp. Proc. 37 (Mater. Res. Soc., Pittsburgh, PA, 1985) p. 41.
[11] K.B. Alexander, C.B. Boothroyd, E.G. Britton, C.S. Baxter, F.M. Ross and W.H. Stobbs, in: Microscopy of Semiconducting Materials 1987, Inst. Phys. Conf. Ser. 87, Ed. A.G. Cullis (Hilger, Bristol, 1987) p. 195.
[12] H. Ichinose, Y. Ishidu, T. Furuta and H. Sakaki, J. Electron Microsc. 36 (1987) 82.
[13] M.P.A. Viegers, A.F. de Jong and M.R. Leys, Spectrochim. Acta 40B (1985) 835.
[14] A.F. de Jong, H. Bender and W. Coene, Ultramicroscopy 21 (1987) 373.
[15] A.F. de Jong, W. Coene and H. Bender, in: Microscopy of Semiconducting Materials 1987, Inst. Phys. Conf. Ser. 87, Ed. A.G. Cullis (Hilger, Bristol, 1987) p. 9.
[16] D. Van Dyck, Advan. Electron. Electron Phys. 65 (1985) 295.
[17] W.O. Saxton, K.M. Knowles and W.M. Stobbs, in: Electron Microscopy and Analysis 1985, Inst. Phys. Conf. Ser. 78, Ed. G.J. Tatlock (Hilger, Bristol, 1985) p. 75.
[18] M.J. Kelly, T.M. Kerr, K.M. Knowles, E.G. Britton, W.M. Stobbs and A.P. Long, J. Appl. Phys., in press.
[19] D.S. Maclagan, L.A. Bursill and A.E.C. Spargo, Phil. Mag. 35 (1977) 757.
[20] W.O. Saxton, T.J. Pitt and M. Horner, Ultramicroscopy 4 (1979) 343.
[21] W.M. Stobbs and W.O. Saxton, J. Microscopy 151 (1988) 171.
[22] R.F. Egerton, Electron Energy Loss Spectroscopy in the Electron Microscope (Plenum, New York, 1986).
[23] W.O. Saxton, J. Microsc. Spectrosc. 5 (1980) 661.
[24] W.O. Saxton and W.M. Stobbs, in: EUREM 84, Budapest, 1984, Eds. A. Csanády, P. Röhlich and D. Szábo (EUREM, Budapest, 1984) p. 287.
[25] H. Kakibayashi and F. Nagata, in: Electron Microscopy 1986, Kyoto, 1986, Eds. T. Imura, S. Maruse and T. Suzuki (Japanese Soc. for Electron Microscopy, Tokyo, 1986) p. 1495.
[26] H. Kakibayashi and F. Nagata, Japan. J. Appl. Phys. 25 (1986) 1644.
[27] W.O. Saxton, W.K. Jenkins, L.A. Freeman and D.J. Smith, Optik 49 (1978) 505.